https://doi.org/10.1016/j.jpowsour.2019.227102

The Thermal Effects of All Porous Solid Oxide Fuel Cells

Haoran Xu[1,2], Bin Chen[1,2*], Peng Tan[2,3], Yuan Zhang[2,4], Qijiao He[2], Zhen Wu[2,5], Meng Ni[2,6*]
[1] Institute of Deep Earth Sciences and Green Energy, Shenzhen University, Shenzhen, 518060, China
[2] Building Energy Research Group, Department of Building and Real Estate
The Hong Kong Polytechnic University, Hung Hom, Kowloon, Hong Kong, China
[3] Department of Thermal Science and Energy Engineering, University of Science and Technology of China, Hefei, 230026, China
[4] State Key Laboratory of Materials-Oriented Chemical Engineering, College of Chemical Engineering, Nanjing Tech University, Nanjing 210009, China
[5] Shaanxi Key Laboratory of Energy Chemical Process Intensification, School of Chemical Engineering and Technology, Xi'an Jiaotong University, Xi'an, China
[6] Environmental Energy Research Group, Research Institute for Sustainable Urban Development (RISUD), The Hong Kong Polytechnic University, Hung Hom, Kowloon, Hong Kong, China

Abstract:

All porous solid oxide fuel cells adopt a porous electrolyte to resist the coking problem when methane is used as the fuel. With the diffusion of O_2 from cathode to anode, various chemical oxidation processes including methane combustion, H_2 combustion and CO combustion occur together with the electrochemical oxidations of H_2 and CO. These reactions release a large amount of heat, thus significantly affects the cell performance. To investigate the thermal effects in the all porous solid oxide fuel cell, a 2D thermal-electrochemical model is developed. Detailed parametric studies are conducted to investigate the effects of applied voltage, inlet gas temperature, electrolyte porosity, and types of supporting layer. Results including power density, oxygen-to-carbon ratio, cell temperature, heat source compositions and species utilization rates are analyzed at different operating conditions. Particularly, this model provides detailed information about the key heat-releasing processes at different operating conditions. A power density of 800 W m^{-2} without the risk of methane coking is obtained using low fuel concentration (4% methane), which can be further improved by increasing fuel concentration and adjusting other proper operating parameters. This model can serve as an effective tool for the optimization of operating conditions and geometry design to improve the performance and coking resistance of solid oxide fuel cells.

Keywords: All porous solid oxide fuel cell; Coking; Carbon deposition; Mathematical modeling; Novel design

---

* Corresponding authors:

Email: chenbinxjtu@gmail.com; Tel: 86-14714939521(Bin Chen)

Email: bsmengni@polyu.edu.hk; Tel: 852-27664152; Fax: 852-27645131 (Meng NI).

1. Introduction

For the sustainable development of human society, clean and high-efficiency energy utilization technologies are urgently demanded [1], such as solid oxide fuel cells (SOFCs) [2]. SOFCs are all solid devices working at high temperature [3]. Usually an SOFC have a sandwich structure with the electrolyte between the anode and cathode [4]. Compared to low temperature fuel cells (e.g. proton exchange membrane fuel cells) [5], SOFCs allow the use of non-noble catalysts [6] and various types of fuels including H_2 [7], CO [8], NH_3 [9], C_nH_m [10], solid carbon [11] and biomass [12]. Among these fuels, CH_4 is especially attractive because it is cheap and has a high volumetric energy density [13]. However, carbon deposition on anode caused by methane decomposition is a severe problem, which deactivates the catalyst and damages the cell [14]. To solve this problem, Guo et al. proposed a new structure by adopting a porous electrolyte sandwiched by a porous anode and a porous cathode, which formed the so called all porous solid oxide fuel cell (AP-SOFC) [15]. In an AP-SOFC, O_2 in cathode side could diffuse through electrolyte to anode and chemically oxidize methane to H_2O and CO_2 [16]. The generated oxidants could further react with methane to generate CO and H_2 by steam reforming and CO_2 reforming and thus inhibited carbon deposition [17]. This method avoided additional auxiliary equipment and successfully achieved a 2000-hour stable operation without carbon deposition on anode in the preliminary experiments [15]. Our previous simulation results revealed the detailed mechanism of AP-SOFCs and proposed promising designs to further improve the performance of AP-SOFCs [18].

However, no detailed thermal-electrochemical analysis has been conducted for AP-SOFCs. A thermal-electrochemical model can provide important information about the effects of operating parameters on temperature distribution of the cell, which is the basis for its long-term stable operation [19]. Moreover, compared with traditional SOFCs, AP-SOFCs generate more waste heat because not only electrochemical oxidations, but also chemical oxidations will generate large amounts of heat [20]. The waste heat of SOFCs can be further utilized to improve the system efficiency when combined with heat engines [21] such as the Otto heat engine [22], organic Rankine cycle [23], Stirling cycle [24] and vacuum thermionic generator [25]. Therefore, this study will be the basis for further studies related with the thermal effects of AP-SOFCs.

2. Model description

A 2D mathematical model coupling mass transport, fluid flow, electrochemical/chemical reactions and heat transfer is developed for a button-type AP-SOFC. The schematic and calculation domains of the AP-SOFC are shown in Fig. 1a and Fig. 1b, respectively. In accordance with the experiments [15], the thicknesses of porous $\mathrm{Gd_{0.1}Ce_{0.9}O_{1.9}}$ (CGO) electrolyte, Ni-CGO anode and $\mathrm{Ba_{0.5}Sr_{0.5}Co_{0.8}Fe_{0.2}O_{3-\delta}}$ (BSCF) cathode are 2 mm, 55 μm and 25 μm, respectively. The active surface area is 2.54 cm^2.

In simulation, N_2-diluted CH_4 and O_2 are introduced into the anode and cathode, respectively. The gas species can flow along the gas channels to the outlet and diffuses through the all porous anode-electrolyte-cathode assembly (AEC) to the other side of the cell. With O_2 molecules transported from the cathode to anode, CH_4 is oxidized by O_2 (methane combustion (MC)) and H_2O is generated. Methane steam reforming (MSR) then occurs, which generates H_2 and CO. Parts of H_2 and CO are directly oxidized by O_2 (combustion (HC) and CO combustion (CC)), the others are electrochemically oxidized by O^{2-} ions. Water gas shift (WGS) reaction is also considered due to the co-existence of H_2O and CO. The direct electrochemical oxidation of CH_4 and dry methane reforming are not considered because their reaction rates are too small compared with existing competitive reactions. Among above mentioned reactions, the electrochemical and chemical oxidations are considered as the main heat sources, while MSR as the main heat sink.

The calculation domains include the anode/cathode chambers and the AEC. Calculations of mass transport, fluid flow and heat transfer are applied to all domains. Chemical reactions including HC, CC and MC are applied to all domains. MSR and WGS reactions are applied to the anode. Electrochemical reactions and ion/electron conductions are applied to the AEC.

Related material properties, kinetic parameters and other tuning parameters can be found in Table 1 and Table 2.

2.1 Model assumptions

To simply the model and keep its accuracy, below assumptions are adopted

(1) The electrochemical reaction area shared by H_2 and CO is proportional to their local mole fractions.

(2) The electrochemical reaction area (triple phase boundaries) are uniformly distributed and the electronic and ionic conducting phases are continuous and assumed to be homogeneous in the porous electrodes as the ionic and electronic conducting materials are well mixed in the electrode preparing.

(3) All the gases are considered as ideal gases because the effects of intermolecular forces and molecules sizes are less significant at high operating temperature.

(4) The ionic conductivity of the porous electrolyte is correlated to its porosity.

2.2 Chemical reactions

Chemical reactions including MC (Eq. (1)), MSR (Eq. (2)), HC (Eq. (3)), CC (Eq. (4)) and WGS (Eq. (5)) are fully considered. The porous electrolyte allows the diffusion of gases between anode and cathode, hence enabling the chemical oxidization of CH_4 as shown in Eq. (1). This reaction inhibits CH_4 decomposition and prevents carbon deposition. Moreover, H_2O is generated from this reaction (Eq. (1)) and MSR is initiated as shown in Eq. (2).

$$\mathrm{CH_4 + 2O_2 = CO_2 + 2H_2O} \tag{1}$$

$$\mathrm{CH_4 + H_2O \leftrightarrow CO + 3H_2} \tag{2}$$

MSR catalyzed by nickel at the anode is a key reaction in AP-SOFCs as it not only inhibits the methane decomposition, but also generates reactive fuels (H_2 and CO) for electrochemical reactions.

The gas diffusion between the anode and cathode also results in the chemical oxidation of H_2 and CO, which needs to be accounted as well:

$$H_2 + 0.5O_2 = H_2O \tag{3}$$

$$CO + 0.5O_2 = CO_2 \tag{4}$$

However, these two reactions are not favored in AP-SOFCs as they reduce the cell efficiency in terms of electricity generation due to the excessive waste heat from them. WGS catalyzed by nickel is also considered as shown in Eq. (5):

$$CO + H_2O \leftrightarrow CO_2 + H_2 \tag{5}$$

The kinetics of above chemical reactions can be found in Table 2.

2.3 Electrochemical reactions

The calculation domains of electrochemical reactions in the model are the whole AEC area. In anode, both H_2 and CO are electrochemically oxidized by O^{2-} ions:

$$H_2 + O^{2-} = H_2O + 2e^- \tag{6}$$

$$CO + O^{2-} = CO_2 + 2e^- \tag{7}$$

The O^{2-} ions are transported from the cathode to anode through electrolyte. In cathode, O_2 molecules are reduced to generate O^{2-} ions:

$$O_2 + 4e^- = 2O^{2-} \tag{8}$$

The overall electrochemical reactions in the cell can be written as Eq. (9) and Eq. (10).

$$H_2 + 0.5O_2 = H_2O \tag{9}$$

$$CO + 0.5O_2 = CO_2 \tag{10}$$

, of which the equilibrium potentials (E_{H_2} and E_{CO}) can be calculated by Eq. (11) and Eq. (12), respectively:

$$E_{H_2} = E_{H_2}^0 + \frac{RT}{2F} \ln \left[\frac{P_{H_2}^L (P_{O_2}^L)^{1/2}}{P_{H_2O}^L} \right] \tag{11}$$

$$E_{CO} = E_{CO}^0 + \frac{RT}{2F} \ln \left[\frac{P_{CO}^L (P_{O_2}^L)^{1/2}}{P_{CO_2}^L} \right] \tag{12}$$

Here R is the universal gas constant, T is the operating temperature and F is the Faraday constant. $P_{H_2}^L$, $P_{H_2O}^L$, P_{CO}^L and $P_{CO_2}^L$ are the anode local gas partial pressures for H_2, H_2O, CO and CO_2, respectively. $P_{O_2}^L$ is the cathode local O_2 partial pressure. $E_{H_2}^0$ and E_{CO}^0 are standard potentials for the electrochemical oxidation of H_2 and CO. Their values can be calculated by Eq. (13) and Eq. (14):

$$E_{H_2}^0 = 1.253 - 0.00024516T \text{ (V)} \tag{13}$$

$$E_{CO}^0 = 1.46713 - 0.0004527T \text{ (V)} \tag{14}$$

The applied voltage of the cell can be calculated by deducting the activation overpotential (η_{act}) and ohmic overpotential (η_{ohmic}) from the equilibrium potential (E_{eq}) as shown in Eq. (15).

$$V = E_{eq} - \eta_{act} - \eta_{ohmic} \tag{15}$$

η_{act} stems from the activation barrier of the electrochemical reactions, which is strongly related with the reactions occurred and the electrode properties. Butler-Volmer equation is adopted to calculate η_{act} as shown in Eq. (16).

$$i = i_0 \left\{ \exp\left(\frac{\alpha n F \eta_{act}}{RT}\right) - \exp\left(-\frac{(1-\alpha) n F \eta_{act}}{RT}\right) \right\} \tag{16}$$

Here i is the operating current density, α is the electron transfer coefficient and n is the number of transferred electrons per mole of electrochemical reaction. The exchange current density (i_0) can be expressed as shown in Eq. (17).

$$i_0 = \gamma\ \exp(-\frac{E_{act}}{RT}) \tag{17}$$

Here γ is the pre-exponential factor and E_{act} is the activation energy. η_{ohmic} is caused by ionic/electronic resistance in the cell and can be calculated by Ohm law. For the electrolyte-supported AP-SOFC, the ionic ohmic loss is the main source of η_{ohmic} and will significantly affect the cell performance. Kinetics of electrochemical reactions above can be found in Table 3.

2.4 Mass transport and fluid flow

The AP-SOFC adopts porous electrolyte, thus mass transport and fluid flow are applied to the whole cell area. In the chambers, free molecular diffusion dominates the mass transport, while Knudsen diffusion becomes significant at AEC area when pore size is comparable to molecular mean-free path. The extended Fick's model is used to calculate mass transport of gas species as shown in Eq. (18) [26].

$$N_i = -\frac{1}{RT}\left(\frac{B_0 y_i P}{\mu}\nabla P - D_i^{eff}\nabla(y_i P)\right)\quad (i = 1, \dots, n) \tag{18}$$

Here B_0 is the permeability, μ is the gas viscosity, y_i is the mole fraction component i and D_i^{eff} is the overall effective diffusion coefficient. D_i^{eff} is determined by Eq. (19) [27].

$$D_i^{eff} = \frac{\varepsilon}{\tau}\left(\frac{1}{D_{im}^{eff}} + \frac{1}{D_{ik}^{eff}}\right)^{-f} \tag{19}$$

, of which ε is the porosity, τ is the tortuosity factor, D_{im}^{eff} is molecular diffusion coefficient and D_{ik}^{eff} is Knudsen diffusion coefficient.

The mass conservation can be described by Eq. (20)

$$\nabla\left(-D_i^{eff}\nabla c_i\right) = R_i \tag{20}$$

The c_i is the gas molar concentration and R_i is the mass source term of the gaseous species.

The general Navier-Stokes equation with Darcy's term is used to calculate the fluid flow as shown in Eq. (21).

$$\rho\frac{\partial u}{\partial t}+\rho u\nabla u=-\nabla p+\nabla[\mu\left(\nabla u+(\nabla u)^{T}\right)-\frac{2}{3}\mu\nabla u\Big]-\frac{\varepsilon\mu u}{k} \tag{21}$$

ρ and u are the gas density and velocity vector, respectively.

2.5 Heat transfer model

In AP-SOFCs, electrochemical/chemical oxidations are the main heat sources and MSR reaction is the main heat sink. In electrochemical oxidations, the heat source includes the irreversible entropy change and reversible overpotential losses. In chemical oxidations, heat released from MC, HC and CC are fully considered.

General heat balance equation is used to calculate the heat transfer as shown in Eq. (22).

$$\rho C_p u\cdot\nabla T+\nabla\cdot\left(-\lambda_{eff}\nabla T\right)=Q \tag{22}$$

Here C_p is the fluid heat capacity at constant pressure, λ_{eff} is the effective thermal conductivity and Q is the general heat source term. In the porous structure of electrodes, λ_{eff} can be corrected by the porosity:

$$\lambda_{eff}=(1-\varepsilon)\lambda_s+\varepsilon\lambda_g \tag{23}$$

Here λ_s and λ_l are the heat conductivities of solid and gaseous phases, respectively. Other related expressions of thermodynamic values for different reactions can be found in Table 4.

2.5 Boundary conditions and model solving

0 V and changeable applied voltage are specified at the outside surface of anode and cathode, respectively. Tunable gas flow rate, species mole fractions and temperature are specified at the chamber inlets. Free flow condition is given at the chamber outlets. At the ends of the cell, zero flux and thermal insulation are specified.

The model is built at given operating parameters such as applied voltage, inlet gas temperature, flow rate and species mole fraction. The governing equations are solved through finite element analysis in the commercial software COMSOL MULTIPHYSICS® v5.3.

3 Results and discussion

3.1 Mesh independence and model validation

Both mesh independence check and model validation between simulation and experiment are conducted before detailed parametric studies. As shown in Fig 1.c, by comparing the simulated current densities at different mesh densities. The mesh density of ca.200000 degrees of freedom is selected for further simulations, as no significant difference is observed beyond this mesh density. The simulated I-V curves at different inlet O_2 mole fractions are also compared with the experimental data [15] as shown in Fig. 1d. In accordance with the experiments, the model employs the same materials, structures and operating parameters. The small difference between experimental data and simulated results validates the model.

After model validation, the effects of various operating parameters such as the applied voltage, inlet gas temperature, inlet gas flow rate and inlet species mole fractions are studied for optimization. By decreasing the thickness of electrolyte and increasing the thickness of anode, the effects of cell structure is also studied.

3.2 Effects of applied voltage

As a basic study, this section adopts the same operating parameters as in experiments except that the inlet gas temperature instead of the cell temperature is directly controlled in the model. In this section, the effects of applied voltage on the performance of AP-SOFCs are studied at given operating parameters (listed in Table 5). The I-V-P curves, minimum anode oxygen-to-carbon ratio (O/C), maximum cell temperature and values of various heat sources at different applied voltages are given in Fig. 2. In Fig. 2(a), the maximum output power density of AP-SOFC reaches 368 W m^{-2} at 0.4 V. This power density is acceptable considering its thick electrolyte (2 mm) and the low mole fraction (0.04) of inlet methane.

According to the fuel cell handbook [28], an O/C value larger than 1.5 on anode surface can effectively prevent carbon deposition caused by methane decomposition. Here one mole CH_4

provides one mole C atom and one mole O_2 and H_2O provide two moles and one mole O atoms, respectively. As shown in Fig. 2(b), the minimum anode O/C value changes between 0.87 and 13.5, where a higher O/C value is obtained at lower applied voltage. The minimum O/C value at anode surface reaches 1.7 when the cell reaches its peak power density. This indicates we can effectively avoid methane coking and achieve long-term stable operation.

The cell temperature is also significantly affected by the applied voltage as shown in Fig. 2(c). The maximum cell temperature changes between 1047 K and 1137 K, which are much higher than the inlet gas temperature (973 K) especially at low applied voltages. A high cell temperature usually brings high electrochemical/chemical reaction activity and results in a higher current density. However, high operating temperature may also damage the stability of cell structure. Therefore, a careful control of cell temperature at low applied voltage is needed to avoid its quick increase.

Heat contributed by different processes are significantly affected by the applied voltage. As shown in Fig. 2(d), the net heat (NH) generation increases from 0.25 W to 0.37 W with the decrease of applied voltage from 0.9 V to 0.1 V. This significant increase of heat generation explains the much higher cell temperature at lower applied voltage as shown in Fig. 2(c). At high applied voltages (0.5 - 0.9 V), most of heat is generated by methane combustion (MC) process, following by the H_2 combustion (HC) and CO combustion (CC) processes. At low applied voltages, heat generated by ohmic overpotential (OO) and activation overpotential (AO) losses has a much larger percentage. This change of percentages of different heat sources indicates the competition between electrochemical oxidation and chemical oxidation reactions. When a safe O/C value is obtained, it is important to find out a set of optimized operating parameters where more O_2 is consumed by electrochemical oxidations rather than chemical oxidations.

3.3 Effect of inlet gas temperature

The working temperature affects not only the safety of long-term operation but also the output power density of the cell. In the model, an indirect strategy (i.e. controlling the inlet gas temperature) is adopted to control the operating temperature of AP-SOFCs. Effects of inlet gas temperature on the cell performance are analysed in this section and related operating parameters can be found in Table 6.

As shown in Fig. 3a, the power density of an AP-SOFC increases quickly from 3 to 358 W m^{-2} with the inlet gas temperature increasing from 823 K to 973 K. The operating temperature of an AP-SOFC is raised along with the increase of inlet gas temperature as shown in Fig. 3b, where the maximum cell temperature increases from 854 K to 1054 K at 823 K and 973 K inlet gas temperatures, respectively. The increase of cell temperature raises the electrochemical and chemical reaction activities and increases the ionic conductivity, thus significantly improves the output power density. The temperature difference between cell and chamber inlet keeps at about 80 K in most of studied parameters, indicating the effective adjustment of cell working temperature by changing the inlet gas temperature.

Moreover, the inlet gas temperature also significantly affects the utilization rate of reactants as shown in Fig. 3c. With the inlet gas temperature increasing from 823 K to 973 K, the utilization rate of O_2 and CH_4 increases from 26% and 24% to 58% and 51%, respectively. The higher utilization rate is contributed by the improved electrochemical/chemical activities, where more heat is generated by electrochemical/chemical oxidations of H_2 and CO instead of CH_4 combustion as shown in Fig. 3d. However, the net heat released is not significantly increased， although more heat released by electrochemical/chemical oxidations between 873 K and 973 K. Because more heat is adsorbed by MSR reaction， which stabilizes the cell temperature.

3.4 Effects of electrolyte porosity

Compared with SOFCs using dense electrolyte, AP-SOFCs provides a special gas-diffusion-layer, the porous electrolyte, to prevent methane coking by introducing O_2 to anode. Obviously, a specific control of O_2 diffusion from cathode to anode is needed because too much O_2 on anode side decreases the power density while inadequate O_2 results in carbon deposition.

Therefore, the porosity of electrolyte that affects diffusion of gas species between anode and cathode is the key factor to be discussed in this section. Related operating parameters can be found in table 7.

As shown in Fig. 4(a), the power density increases from 168 W m^{-2} to 596 W m^{-2} with the electrolyte porosity decreasing from 0.6 to 0.2. However, the O/C value decreases from1.86 to 0.97 with the decrease of porosity from 0.6 to 0.2. The trade-off between power density and safety operation is thus needed to be considered in this situation.

With the increase of electrolyte porosity, more CH_4 and O_2 are utilized as shown in Fig. 4(b). The utilization rates for O_2 and CH_4 increase from 50% and 45% to 62% and 53% at electrolyte porosities being 0.2 and 0.6, respectively. Although more fuel and oxidants are consumed at higher porosity cases, the more chemical energy is converted to heat instead of electricity power. As shown in Fig. 4(c), heat generated from CH_4/H_2/CO combustions keeps growing, while heat generated from electrochemical reactions keeps decreasing with the increase of electrolyte porosity. As a result, the power density decreases while the maximum cell temperature increases from 1033 K at a porosity of 0.2 to 1067 K at 0.6 porosity as shown in Fig 4(d).

3.5 Effects of support-layer type

In experiments [15], electrolyte-supported (ES) AP-SOFC is adopted. Compared with electrolyte-supported type, anode-supported (AS) SOFC usually has less ohmic overpotential losses and shows better electrochemical performance [29]. In this section, the structure of AP-SOFC is modified from electrolyte-supported type to anode-supported type, of which the electrolyte and anode are changed from 2 mm and 0.055 mm to 1 mm and 1.055mm in thickness, respectively. Related operating parameters can be found in Table 8.

As shown in Fig. 5(a), the anode-supported type reaches a peak power density of 800 W m^{-2}, which is almost twice of the electrolyte-supported type (439 W m^{-2}). In addition, the anode-supported type has a higher O/C value at most applied voltages (0.2–0.9 V) as shown in Fig. 5(b). Although the cell temperature (Fig. 5(c)) and net heat generation (Fig. 5(d)) are very close at most applied voltages, these two types have very different percentages regarding heat sources. Compared with the electrolyte-supported type, the anode-supported type releases more heat from activation overpotential loss and adsorbs more heat in MSR process. On the other hand, less heat from H_2/CO combustion is generated in the anode-supported type especially at small applied voltages (0.1–0.5 V), indicating the priority for electrochemical oxidations in anode-supported type when competing against chemical oxidations.

4 Conclusion

A numerical model fully considering the electrochemical/chemical reactions, mass/momentum transport and heat transfer was developed to study the thermal effects in the all porous solid oxide fuel cells (AP-SOFC). Detailed parametric studies were conducted for various operating parameters (e.g. applied voltage, inlet gas temperature, inlet gas species) and different cell structures (e.g. electrolyte porosity and electrolyte/anode thickness). Performance indicators of the cell such as the output power density, the O/C value and maximum cell temperature were discussed for parameter optimization.

From the parametric studies, it was found that the peak power density of an AP-SOFC was significantly affected by the inlet gas temperature, electrolyte porosity and supporting layer (anode-supported vs. electrolyte-supported). Detailed analysis revealed that the inlet gas temperature affected the activity of electrochemical/chemical reactions and the ionic conductivity. Adjusting inlet gas temperature could effectively control the cell operating temperature, reactant utilization rates and heat released by various heat sources. Moreover, a small electrolyte porosity would raise the power density of the cell and decrease the waste heat due to the depressed chemical oxidation reactions. Nevertheless, a small electrolyte porosity decreased O/C value at anode, which could result in methane coking in long-term operation. By modifying the anode and electrolyte thickness, the performance of anode-supported and electrolyte-supported AP-SOFCs were compared. The anode-supported AP-SOFC showed a higher peak power density (439 W m^{-2} vs 800 W m^{-2}) and larger anode O/C value at most applied voltages (0.2–0.8 V) than the electrolyte-supported one. The percentages of various heat sources were also affected by the supporting type, where the anode-supported type generated more heat from electrochemical reactions while the electrolyte-supported type generated more heat from chemical oxidations.

Acknowledgement

M. Ni thanks the grant (Project Number: PolyU 152214/17E and PolyU 152064/18E) from Research Grant Council, University Grants Committee, Hong Kong SAR. P. Tan thanks the funding support from CAS Pioneer Hundred Talents Program. Z. Wu thanks the funding support from the National Natural Science Foundation of China (No. 21736008) and the Hong Kong Scholar Program (No. XJ2017023)

Nomenclatures

Abbreviations

AEC	Anode-electrolyte-cathode assembly
AP-SOFC	All porous solid oxide fuel cell
BSCF	Barium strontium cobalt ferrite ($\mathrm{Ba_{0.5}Sr_{0.5}Co_{0.8}Fe_{0.2}O_{3-\delta}}$)
CC	Carbon monoxide combustion
CGO	gadolinium-doped ceria ($\mathrm{Gd_{0.1}Ce_{0.9}O_{1.9}}$)
HC	Hydrogen combustion
MC	Methane combustion
MSR	Methane steam reforming
O/C	Oxygen to carbon ratio
SCCM	Standard cubic centime per minute
SOFC	Solid oxide fuel cell
WGS	Water gas shift

Roman

B_0	Permeability coefficient, m^2

c_{CO_2}	Mole concentration of carbon dioxide, mol·m^{-3}
c_{H_2O}	Mole concentration of water, mol·m^{-3}
C_p	Heat capacity at constant pressure
D_i^{eff}	Effective diffusivity of species i , m^2·s^{-1}
D_{ik}^{eff}	Knudsen diffusion coefficient of i , m^2·s^{-1}
D_{im}^{eff}	Molecular diffusion coefficient of i, m^2·s^{-1}
E_{act}	Activation energy, J·mol^{-1}
E_{CO}	Equilibrium potential for carbon monoxide oxidization, V
E_{CO}^0	Standard equilibrium potential for carbon monoxide oxidization, V
E_{eq}	Equilibrium Nernst potential, V
E_{H_2}	Equilibrium potential for hydrogen oxidization, V
$E_{H_2}^0$	Standard equilibrium potential for hydrogen oxidization, V
F	Faraday constant, 96485 C·mol^{-1}
i	Operating current density, A·m^{-2}
i_o	Exchange current density, A·m^{-2}
n	Number of electrons transferred per electrochemical reaction
N_i	Flux of mass transport, kg·m^{-3}·s^{-1}
p	(partial) Pressure, Pa
P_{CO}^L	Local CO partial pressures, Pa
$P_{CO_2}^L$	Local CO_2 partial pressures, Pa
$P_{H_2}^L$	Local H_2 partial pressures, Pa
$P_{H_2O}^L$	Local H_2O partial pressures, Pa
$P_{O_2}^L$	Local O_2 partial pressures, Pa
R	Gas constant, 8.314 J·mol^{-1}·K^{-1}
R_{CMO}	Carbon monoxide oxidization reaction
R_{HO}	Hydrogen oxidization reaction
R_{MSR}	Methane steam reforming reaction

R_{MO}	Methane oxidization reaction
R_{WGS}	Water gas shift reaction
T	Temperature, K
u	Velocity field, $m^3 \cdot s^{-1}$
V	Volume fraction
y_i	Mole fraction of component i

Greek letters

α	Charge transfer coefficient
ε	Porosity
η_{act}	Activation overpotential loss, V
η_{ohmic}	Ohmic overpotential loss, V
κ	Permeability, m^2
λ	Heat conductivity
μ	Dynamic viscosity of fluid, Pa·s
ρ	Fluid density, $kg \cdot m^{-3}$
σ	Conductivity, S/m
γ	Pre-exponential factor, A m^{-2}
τ	Tortuosity

Subscripts

an	Anode
ca	Cathode
CH_4	Methane
CO	Carbon monoxide
CO_2	Carbon dioxide
el	Electrolyte
H_2	Hydrogen

l	Ionic phase
O_2	Oxygen
s	Electronic phase

Superscripts

0	Parameter at equilibrium conditions
eff	Effective
L	Local

Reference

[1] Li W, Lu C. The multiple effectiveness of state natural gas consumption constraint policies for achieving sustainable development targets in China. Appl Energy 2019;235:685–98. doi:https://doi.org/10.1016/j.apenergy.2018.11.013.

[2] Park S, Vohs JM, Gorte RJ. Direct oxidation of hydrocarbons in a solid-oxide fuel cell. Nature 2000;404:265–7.

[3] Ormerod RM. Solid oxide fuel cells. Chem Soc Rev 2003;32:17–28. doi:10.1039/B105764M.

[4] Gu Y, Zhang Y, Ge L, Zheng Y, Chen H, Guo L. YSZ electrolyte support with novel symmetric structure by phase inversion process for solid oxide fuel cells. Energy Convers Manag 2018;177:11–8. doi:https://doi.org/10.1016/j.enconman.2018.09.051.

[5] Wu H-W. A review of recent development: Transport and performance modeling of PEM fuel cells. Appl Energy 2016;165:81–106. doi:https://doi.org/10.1016/j.apenergy.2015.12.075.

[6] Shi Y, Cai N, Li C, Bao C, Croiset E, Qian J, et al. Modeling of an anode-supported Ni–YSZ|Ni–ScSZ|ScSZ|LSM–ScSZ multiple layers SOFC cell: Part I. Experiments, model development and validation. J Power Sources 2007;172:235–45. doi:http://dx.doi.org/10.1016/j.jpowsour.2007.04.037.

[7] Eriksson EL V, Gray EM. Optimization and integration of hybrid renewable energy

hydrogen fuel cell energy systems – A critical review. Appl Energy 2017;202:348–64. doi:https://doi.org/10.1016/j.apenergy.2017.03.132.

[8] Singhal SC. Advances in solid oxide fuel cell technology. Solid State Ionics 2000;135:305–13. doi:http://dx.doi.org/10.1016/S0167-2738(00)00452-5.

[9] Perna A, Minutillo M, Jannelli E, Cigolotti V, Nam SW, Han J. Design and performance assessment of a combined heat, hydrogen and power (CHHP) system based on ammonia-fueled SOFC. Appl Energy 2018;231:1216–29. doi:https://doi.org/10.1016/j.apenergy.2018.09.138.

[10] Chen B, Xu H, Tan P, Zhang Y, Xu X, Cai W, et al. Thermal modelling of ethanol-fuelled Solid Oxide Fuel Cells. Appl Energy 2019;237:476–86. doi:https://doi.org/10.1016/j.apenergy.2019.01.025.

[11] Xu H, Chen B, Zhang H, Sun Q, Yang G, Ni M. Modeling of direct carbon solid oxide fuel cells with H2O and CO2as gasification agents. Int J Hydrogen Energy 2017;42:15641–51. doi:10.1016/j.ijhydene.2017.05.075.

[12] Sharma M, N R, Dasappa S. Solid oxide fuel cell operating with biomass derived producer gas: Status and challenges. Renew Sustain Energy Rev 2016;60:450–63. doi:https://doi.org/10.1016/j.rser.2016.01.075.

[13] Gür TM. Comprehensive review of methane conversion in solid oxide fuel cells: Prospects for efficient electricity generation from natural gas. Prog Energy Combust Sci 2016;54:1–64. doi:http://dx.doi.org/10.1016/j.pecs.2015.10.004.

[14] Yang L, Wang SZ, Blinn K, Liu MF, Liu Z, Cheng Z, et al. Enhanced Sulfur and Coking Tolerance of a Mixed Ion Conductor for SOFCs: BaZr0.1Ce0.7Y0.2-xYbxO3-delta. Science (80-) 2009;326:126–9.

[15] Guo Y, Bessaa M, Aguado S, Steil MC, Rembelski D, Rieu M, et al. An all porous solid oxide fuel cell (SOFC): a bridging technology between dual and single chamber SOFCs. Energy Environ Sci 2013;6:2119–23. doi:10.1039/C3EE40131F.

[16] Guo YM, Largiller G, Guizard C, Tardivat C, Farrusseng D. Coke-free operation of an all porous solid oxide fuel cell (AP-SOFC) used as an O2 supply device. J Mater Chem

A 2015;3:2684–9. doi:10.1039/C4TA05009F.

[17] Xie Y, Ding H, Xue X. Direct methane fueled solid oxide fuel cell model with detailed reforming reactions. Chem Eng J 2013;228:917–24. doi:http://dx.doi.org/10.1016/j.cej.2013.05.084.

[18] Xu H, Chen B, Tan P, Xuan J, Maroto-Valer MM, Farrusseng D, et al. Modeling of all-porous solid oxide fuel cells with a focus on the electrolyte porosity design. Appl Energy 2019;235:602–11. doi:https://doi.org/10.1016/j.apenergy.2018.10.069.

[19] Ni M. Thermo-electrochemical modeling of ammonia-fueled solid oxide fuel cells considering ammonia thermal decomposition in the anode. Int J Hydrogen Energy 2011;36:3153–66. doi:http://dx.doi.org/10.1016/j.ijhydene.2010.11.100.

[20] Xu H, Chen B, Tan P, Cai W, He W, Farrusseng D, et al. Modeling of all porous solid oxide fuel cells. Appl Energy 2018;219:105–13. doi:10.1016/j.apenergy.2018.03.037.

[21] Zhang H, Xu H, Chen B, Dong F, Ni M. Two-stage thermoelectric generators for waste heat recovery from solid oxide fuel cells. Energy 2017;132:280–8. doi:10.1016/j.energy.2017.05.005.

[22] Xu H, Chen B, Tan P, Zhang H, Yuan J, Irvine JTS, et al. Performance improvement of a direct carbon solid oxide fuel cell through integrating an Otto heat engine. Energy Convers Manag 2018;165:761–70. doi:10.1016/j.enconman.2018.04.008.

[23] Eveloy V, Karunkeyoon W, Rodgers P, Al Alili A. Energy, exergy and economic analysis of an integrated solid oxide fuel cell – gas turbine – organic Rankine power generation system. Int J Hydrogen Energy 2016;41:13843–58. doi:https://doi.org/10.1016/j.ijhydene.2016.01.146.

[24] Xu H, Chen B, Tan P, Zhang H, Yuan J, Liu J, et al. Performance improvement of a direct carbon solid oxide fuel cell system by combining with a Stirling cycle. Energy 2017;140:979–87. doi:10.1016/j.energy.2017.09.036.

[25] Xu H, Chen B, Tan P, Cai W, Wu Y, Zhang H, et al. A feasible way to handle the heat management of direct carbon solid oxide fuel cells. Appl Energy 2018;226:881–90. doi:https://doi.org/10.1016/j.apenergy.2018.06.039.

[26] Suwanwarangkul R, Croiset E, Fowler MW, Douglas PL, Entchev E, Douglas MA. Performance comparison of Fick's, dusty-gas and Stefan–Maxwell models to predict the concentration overpotential of a SOFC anode. J Power Sources 2003;122:9–18. doi:http://dx.doi.org/10.1016/S0378-7753(02)00724-3.

[27] Kong W, Zhu H, Fei Z, Lin Z. A modified dusty gas model in the form of a Fick's model for the prediction of multicomponent mass transport in a solid oxide fuel cell anode. J Power Sources 2012;206:171–8. doi:http://dx.doi.org/10.1016/j.jpowsour.2012.01.107.

[28] NETL. Fuel Cell Handbook, Seventh Edition. DOE/NETL; 2004.

[29] Xu H, Chen B, Liu J, Ni M. Modeling of direct carbon solid oxide fuel cell for CO and electricity cogeneration. Appl Energy 2016;178:353–62. doi:10.1016/j.apenergy.2016.06.064.

[30] Jin W, Gu X, Li S, Huang P, Xu N, Shi J. Experimental and simulation study on a catalyst packed tubular dense membrane reactor for partial oxidation of methane to syngas. Chem Eng Sci 2000;55:2617–25. doi:http://dx.doi.org/10.1016/S0009-2509(99)00542-4.

[31] Ni M, Leung DYC, Leung MKH. Modeling of methane fed solid oxide fuel cells: Comparison between proton conducting electrolyte and oxygen ion conducting electrolyte. J Power Sources 2008;183:133–42. doi:http://dx.doi.org/10.1016/j.jpowsour.2008.04.073.

[32] Ni M. 2D thermal modeling of a solid oxide electrolyzer cell (SOEC) for syngas production by H2O/CO2 co-electrolysis. Int J Hydrogen Energy 2012;37:6389–99. doi:10.1016/j.ijhydene.2012.01.072.

List of Tables

Table 1 Material properties

Parameters	**Value or expression**	**Unit**
Conductivity		
$\boldsymbol{\sigma}_{\mathbf{CGO}}$	$(3.34-7.18\varepsilon+3.84\varepsilon^2)\times\frac{100}{T}\times e^{(-\frac{10670}{T}+13.755)}$	S m^{-1}
$\boldsymbol{\sigma}_{\mathbf{BSCF}}$	$-24455+82.321T-\frac{8.28T^2}{1000}+\frac{2.7778T^3}{10000}$	S m^{-1}
$\boldsymbol{\sigma}_{\mathbf{Ni}}$	$3.27\times10^6-1065.3T$	S m^{-1}
Porosity		
$\boldsymbol{\varepsilon}_{\mathbf{an}}$	0.6	
$\boldsymbol{\varepsilon}_{\mathbf{ca}}$	0.6	
$\boldsymbol{\varepsilon}_{\mathbf{el}}$	0.2-0.6	
Anode volume fraction		
$\boldsymbol{V}_{\mathbf{CGO}}$	0.23	
$\boldsymbol{V}_{\mathbf{Ni}}$	0.77	
Cathode volume fraction		
$\boldsymbol{V}_{\mathbf{CGO}}$	0.25	
$\boldsymbol{V}_{\mathbf{BSCF}}$	0.75	
Electrode tortuosity		
$\boldsymbol{\tau}_{\mathbf{an}}$	3	
$\boldsymbol{\tau}_{\mathbf{ca}}$	3	

Table 2 Kinetic parameters for chemical reactions

Reaction	**Unit**
Methane oxidization reaction rate [30]	
$5 \times 10^4 \times e^{\frac{-166000}{RT}} \times p_{CH_4} \times p_{O_2}$ (anode)	$mol\ \ m^3\ \ s^{-1}$
$1.1 \times e^{\frac{-166000}{RT}} \times p_{CH_4} \times p_{O_2}$ (other area)	$mol\ \ m^3\ \ s^{-1}$
Hydrogen oxidization reaction rate [30]	
$5 \times 10^4 \times e^{\frac{-48484}{RT}} \times p_{CH_4} \times p_{O_2}^{0.5}$	$mol\ \ m^3\ \ s^{-1}$
Carbon monoxide oxidization reaction rate [30]	
$5 \times 10^4 \times e^{\frac{-47773}{RT}} \times p_{CO} \times p_{O_2}^{0.5}$	$mol\ \ m^3\ \ s^{-1}$
Methane steam reforming reaction rate [31]	
$2.395 \times 10^7 \times e^{\frac{-231266}{RT}} \times (p_{CH_4} \times p_{H_2O} - \frac{p_{CH_4}^3 \times p_{CO}}{K_{pr}})$	$mol\ \ m^3\ \ s^{-1}$
$K_{pr} = 1.0267 \times 10^{10} \times e^{-0.2513 \times Z^4 + 0.3665 \times Z^3 + 0.5810 \times Z^2 - 27.134 \times Z + 3.277}$	
$Z = \frac{T}{1000}$	
Water gas shift reaction rate [32]	
$0.0171 \times e^{\frac{-103191}{RT}} \times (p_{CO} \times p_{H_2O} - \frac{p_{H_2} \times p_{CO_2}}{k_{ps}})$	$mol\ \ m^3\ \ s^{-1}$
$k_{ps} = e^{-0.2935 \times Z^3 + 0.6351 \times Z^2 + 4.1788 \times Z + 0.0169}$	
$Z = \frac{T}{1000}$	

Table 3 Kinetic parameters electrochemical reaction

Parameter	**Value**	**Unit**

γ_{H_2}	3.68×10^9	A m^{-2}
E_{act,H_2}	1.2×10^5	J mol^{-1}
γ_{O_2}	1.39×10^{10}	A m^{-2}
E_{act,O_2}	1.2×10^5	J mol^{-1}
γ_{CO}	1.67×10^9	A m^{-2}
$E_{act,CO}$	1.2×10^5	J mol^{-1}
α_{H_2}	0.5	
α_{CO}	0.5	
α_{O_2}	0.5	

Table 4 Thermodynamic values of different reactions

Reaction	**Value**	**Unit**
$CH_4 + 2O_2 = CO_2 + 2H_2O$	$dH = -794.99198 - 0.00642T$	kJ
$H_2 + 0.5O_2 = H_2O$	$dH = -241.3 - 0.00634T$	kJ
	$dS = -48.40129 - 0.00642T$	J/K
$CO + 0.5O_2 = CO_2$	$dH = -286.27752 + 0.00374T$	kJ
	$dS = -90.6742 + 0.00364T$	J/K
$CH_4 + H_2O \leftrightarrow CO + 3H_2$	$dH = 251.18556 + 0.00887T$	kJ
$CO + H_2O \leftrightarrow CO_2 + H_2$	$dH = -44.97751 + 0.01008T$	kJ

Table 5 Operation parameters for basic case study of all porous solid oxide fuel cells

Parameter	**Value**	**Unit**
Operating potential	0 – 0.9	V
Inlet gas flow rate	100	SCCM
Anode inlet gas composition	4% CH_4 + 96% N_2 in volume	
Cathode inlet gas composition	4% O_2 + 96 N_2%	
Inlet gas temperature	973	K
Electrolyte porosity	0.42	
Support type	Electrolyte supported	

Table 6 Operation parameters in studying effects of inlet gas temperature

Parameter	**Value**	**Unit**
Operating potential	0.5	V
Inlet gas flow rate	100	SCCM
Anode inlet gas composition	4% CH_4 + 96% N_2 in volume	
Cathode inlet gas composition	4% O_2 + 96% N_2 in volume	
Inlet gas temperature	823–973	K
Electrolyte porosity	0.42	
Support type	Electrolyte supported	

Table 7 Operation parameters in studying effects of electrolyte porosity

Parameter	**Value**	**Unit**
Operating potential	0.5	V
Inlet gas flow rate	100	SCCM
Anode inlet gas composition	4% CH_4 + 96% N_2 in volume	
Cathode inlet gas composition	4% O_2 + 96% N_2 in volume	
Inlet gas temperature	973	K
Electrolyte porosity	0.2–0.6	
Support type	Electrolyte supported	

Table 8 Operation parameters in studying effects of support type

Parameter	**Value**	**Unit**
Operating potential	0–0.9	V
Inlet gas flow rate	100	SCCM
Anode inlet gas composition	4% CH_4 + 96% N_2 in volume	
Cathode inlet gas composition	4% O_2 + 96% N_2 in volume	
Inlet gas temperature	973	K
Electrolyte porosity	0.42	
Support type	Electrolyte supported, anode supported	

List of Figures

Fig.1 (a)Schematic of a button all-porous solid oxide fuel cell; (b) Calculation domains for different chemical/physical processes; (c) Mesh independence validation; (d) Model validation for the button all-porous solid oxide fuel cell at different cathode inlet O_2 mole fractions.

Fig. 2 (a) The I-V-P characteristics of an all porous solid oxide fuel cell; (b) Anode surface O/C values at different applied voltages; (c) Maximum cell temperatures at different applied voltages; (d) Comparison of heat sources including methane steam reforming (MSR), anode overpotential (AO), ohmic overpotential (OO), H_2 combustion (HC), CO combustion (CC) and methane combustion (MC) and net heat (NH) generation at different applied voltages.

Fig. 3 (a) Output power densities at different inlet gas temperature; (b) Comparison between maximum cell temperatures and inlet gas temperatures; (c) Utilization rates of O_2 and CH_4 at different inlet gas temperatures; (d) Comparison of heat sources including methane steam reforming (MSR), anode overpotential (AO), ohmic overpotential (OO), H_2 combustion (HC), CO combustion (CC) and methane combustion (MC) and net heat (NH) generation at different inlet gas temperatures.

Fig. 4 (a) Output power densities and minimum anode O/C values at different electrolyte porosities; (b) Utilization rates of O_2 and CH_4 at different electrolyte porosities; (c) Comparison of heat sources including methane steam reforming (MSR), anode overpotential (AO), ohmic overpotential (OO), H_2 combustion (HC), CO combustion (CC) and methane combustion (MC) and net heat (NH) generation at different electrolyte porosities; (d) Maximum cell temperatures at different electrolyte porosities;

Fig. 5 Comparison of I-V-P characteristics between the electrolyte-supported (ES) and anode-supported (AS) all porous solid oxide fuel cells; (b) Comparison of minimum anode O/C values between the electrolyte-supported (ES) and anode-supported at different applied voltages(AS) all porous solid oxide fuel cells; (c) Comparison of maximum cell temperatures between the electrolyte-supported (ES) and anode-supported (AS) all porous solid oxide fuel cells at different applied voltages; (d) Comparison of heat sources including methane steam reforming (MSR), anode overpotential (AO), ohmic overpotential (OO), H_2 combustion (HC), CO combustion (CC) and methane combustion (MC) and net heat (NH) generation between the electrolyte-supported (ES) and anode-supported (AS) all porous solid oxide fuel cells at different applied voltages.

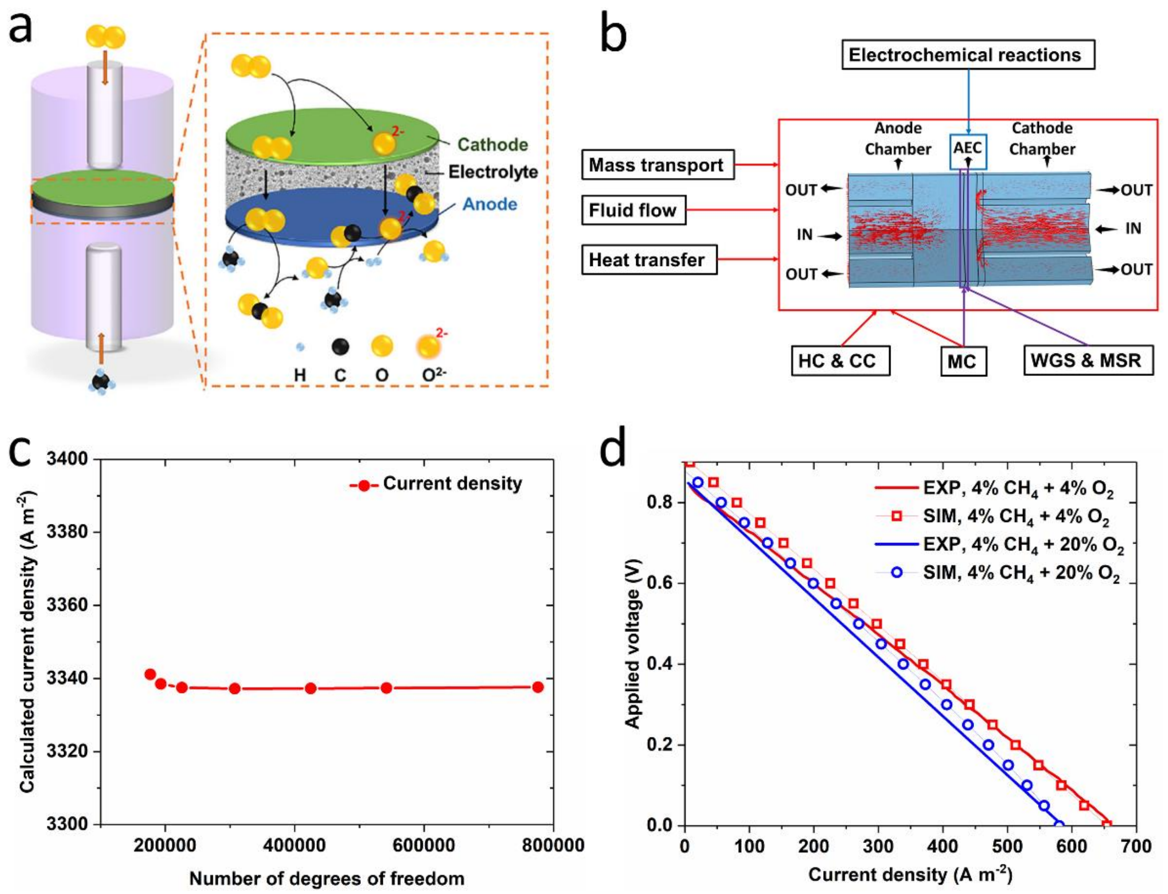

Fig.1 (a)Schematic of a button all-porous solid oxide fuel cell; (b) Calculation domains for different chemical/physical processes; (c) Mesh independence validation; (d) Model validation for the button all-porous solid oxide fuel cell at different cathode inlet O_2 mole fractions.

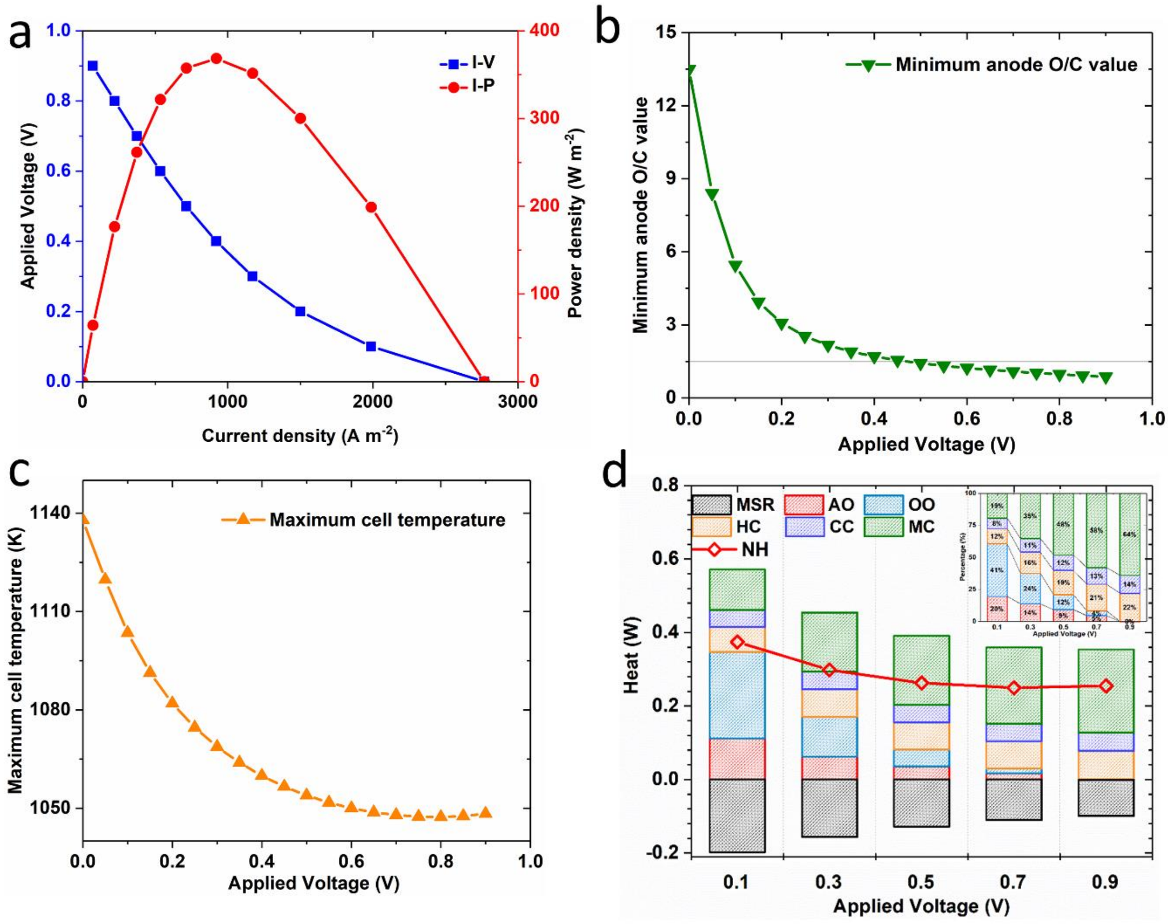

Fig. 2 (a) The I-V-P characteristics of an all porous solid oxide fuel cell; (b) Anode surface O/C values at different applied voltages; (c) Maximum cell temperatures at different applied voltages; (d) Comparison of heat sources including methane steam reforming (MSR), anode overpotential (AO), ohmic overpotential (OO), H_2 combustion (HC), CO combustion (CC) and methane combustion (MC) and net heat (NH) generation at different applied voltages.

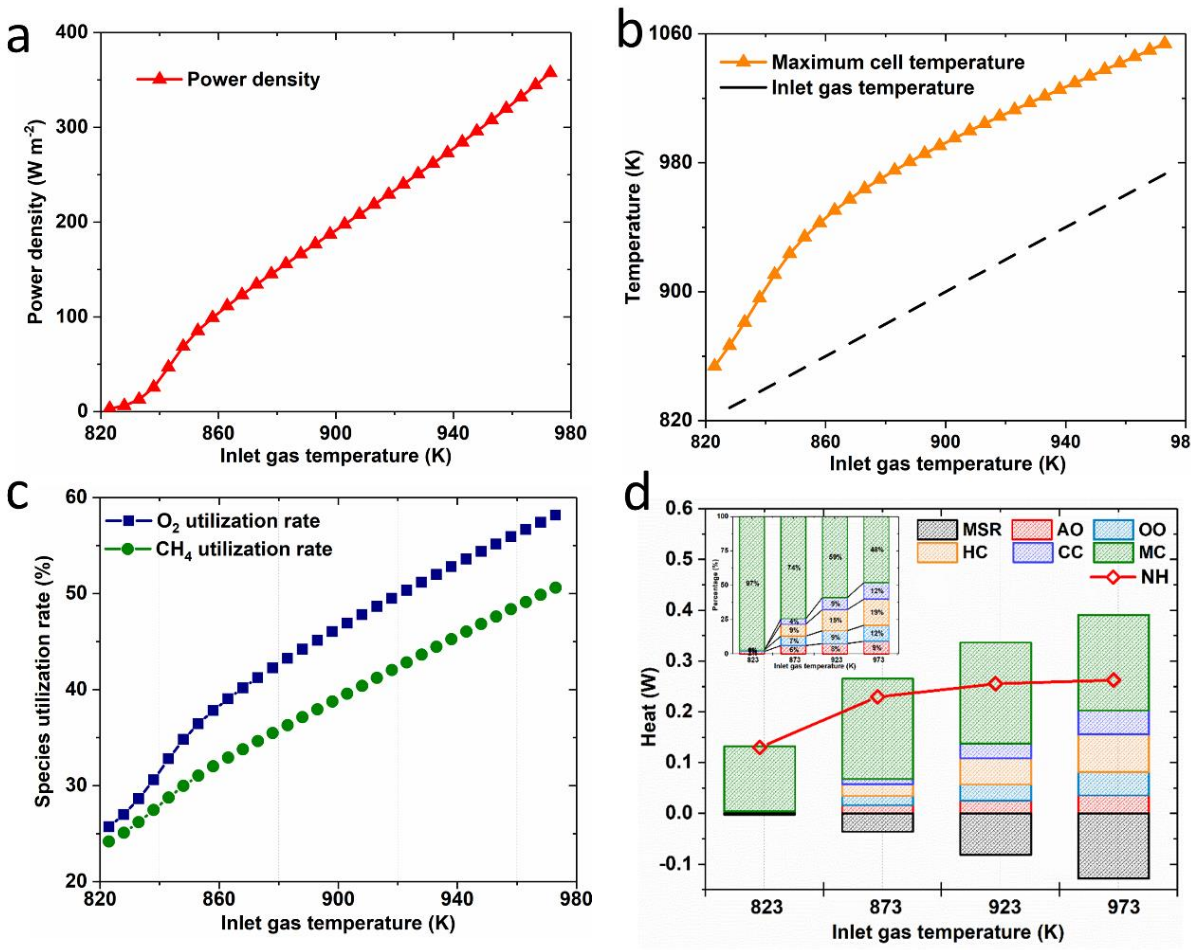

Fig. 3 (a) Output power densities at different inlet gas temperature; (b) Comparison between maximum cell temperatures and inlet gas temperatures; (c) Utilization rates of O_2 and CH_4 at different inlet gas temperatures; (d) Comparison of heat sources including methane steam reforming (MSR), anode overpotential (AO), ohmic overpotential (OO), H_2 combustion (HC), CO combustion (CC) and methane combustion (MC) and net heat (NH) generation at different inlet gas temperatures.

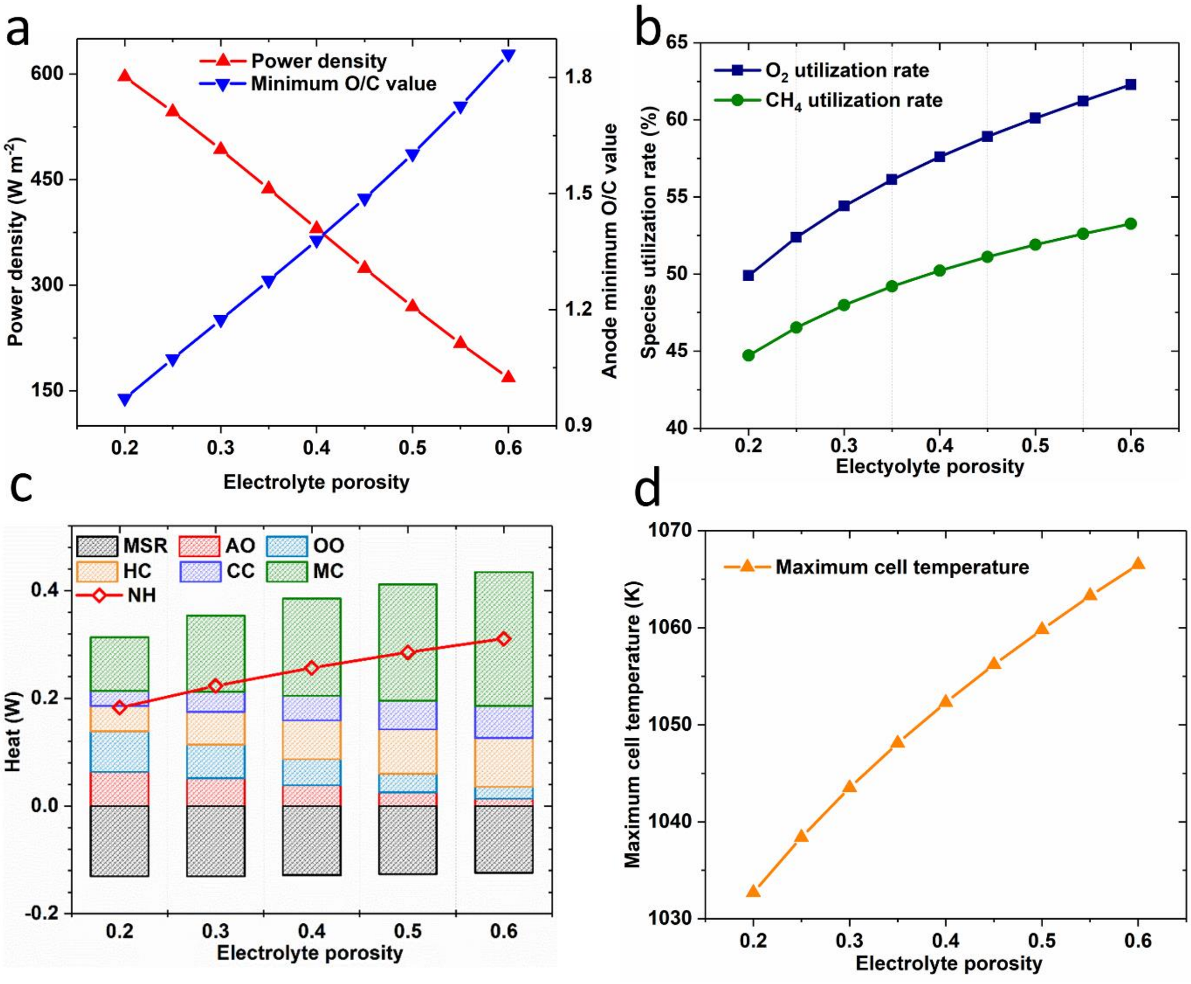

Fig. 4 (a) Output power densities and minimum anode O/C values at different electrolyte porosities; (b) Utilization rates of O_2 and CH_4 at different electrolyte porosities; (c) Comparison of heat sources including methane steam reforming (MSR), anode overpotential (AO), ohmic overpotential (OO), H_2 combustion (HC), CO combustion (CC) and methane combustion (MC) and net heat (NH) generation at different electrolyte porosities; (d) Maximum cell temperatures at different electrolyte porosities;

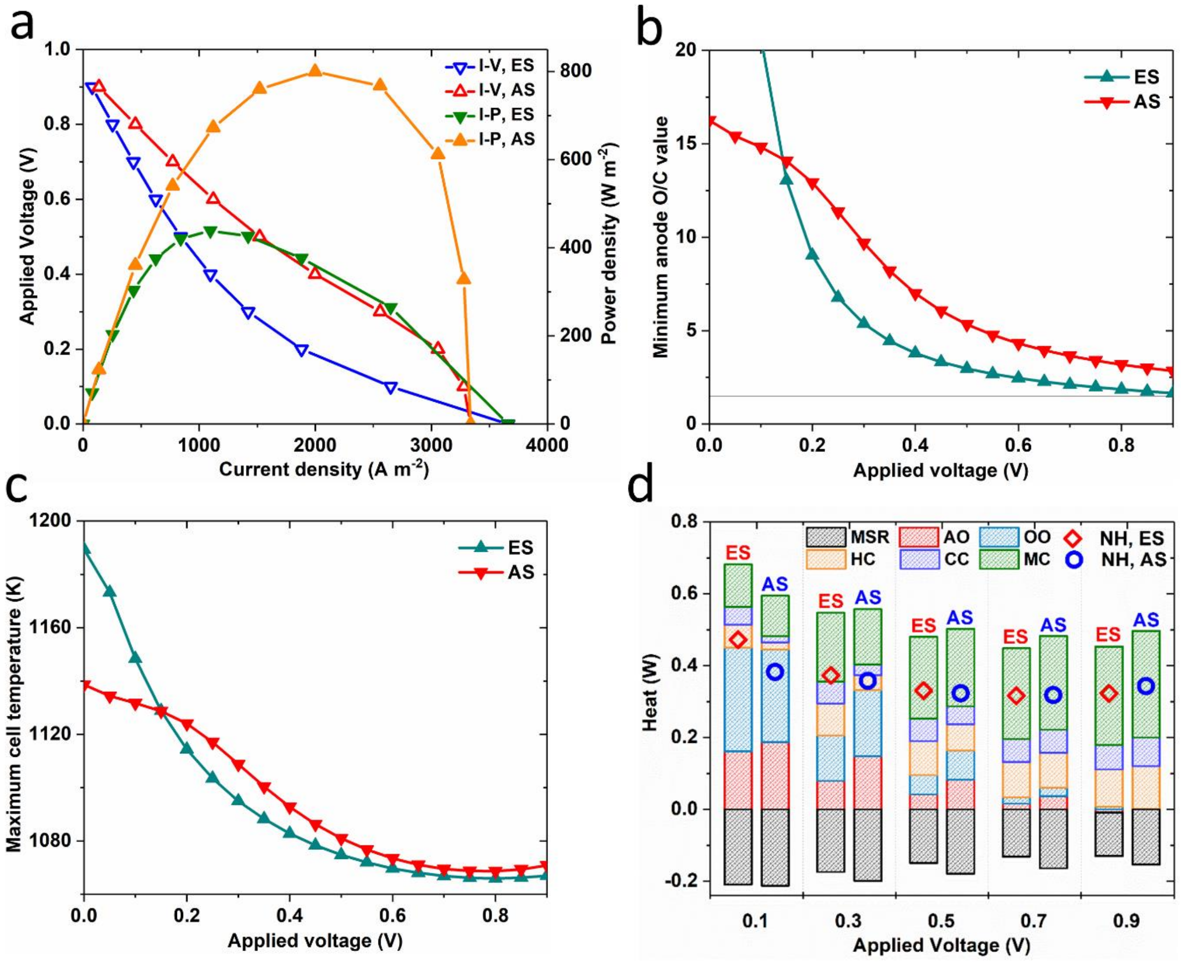

Fig. 5 Comparison of I-V-P characteristics between the electrolyte-supported (ES) and anode-supported (AS) all porous solid oxide fuel cells; (b) Comparison of minimum anode O/C values between the electrolyte-supported (ES) and anode-supported at different applied voltages(AS) all porous solid oxide fuel cells; (c) Comparison of maximum cell temperatures between the electrolyte-supported (ES) and anode-supported (AS) all porous solid oxide fuel cells at different applied voltages; (d) Comparison of heat sources including methane steam reforming (MSR), anode overpotential (AO), ohmic overpotential (OO), H_2 combustion (HC), CO combustion (CC) and methane combustion (MC) and net heat (NH) generation between the electrolyte-supported (ES) and anode-supported (AS) all porous solid oxide fuel cells at different applied voltages.